

One-bright-two-dark ring solitons of partially directional nonlocal three-component nonlinear Schrodinger model

Ru-Meng Zhao(赵汝孟), Rui-Jie Li(李瑞杰), Shu-Yi Li(李书艺), Jing Yang(杨静), Ji-Tao Li(理记涛)
Citation: Chin. Phys. B. 35, 090503 (2026). DOI: 10.1088/1674-1056/ae521b | CSTR: 32038.14.CPB.ae521b
http://cpb.iphy.ac.cn; http://iopscience.iop.org/cpb

What follows is a list of articles you may be interested in

Periodic lump, soliton, and some mixed solutions of the (2+1)-dimensional generalized coupled nonlinear Schrödinger equations

Xiao-Min Wang(王晓敏), Ji Li(李吉), Xiao-Xiao Hu(胡霄骁)
Chin. Phys. B. 34, 110502 (2025). DOI: 10.1088/1674-1056/ae1019 | CSTR: 32038.14.CPB.ae1019

Effective regulation of the interaction process among three optical solitons

Houhui Yi(伊厚会), Xiaofeng Li(李晓凤), Junling Zhang(张俊玲), Xin Zhang(张鑫), Guoli Ma(马国利)
Chin. Phys. B. 33, 100502 (2024). DOI: 10.1088/1674-1056/ad6b87

Parametric instability in the pure-quartic nonlinear Schrödinger equation

Yun-Hong Zhang(张云红), Chong Liu(刘冲)
Chin. Phys. B. 33, 030506 (2024). DOI: 10.1088/1674-1056/ad11e7

Dual-wavelength pumped latticed Fermi–Pasta–Ulam recurrences in nonlinear Schrödinger equation

Qian Zhang(张倩), Xiankun Yao(姚献坤), Heng Dong(董恒)
Chin. Phys. B. 33, 030502 (2024). DOI: 10.1088/1674-1056/ad181e

Influence of the initial parameters on soliton interaction in nonlinear optical systems

Xinyi Zhang(张昕仪), Ye Wu(吴晔)
Chin. Phys. B. 32, 070505 (2023). DOI: 10.1088/1674-1056/ace1da

---

SPECIAL TOPIC — Nonlinear localized waves: Theory, methods and applications

One-bright-two-dark ring solitons of partially directional nonlocal three-component nonlinear Schrödinger model

Ru-Meng Zhao(赵汝孟), Rui-Jie Li(李瑞杰), Shu-Yi Li(李书艺), Jing Yang(杨静)[†], and Ji-Tao Li(理记涛)[‡]

School of Physics and Telecommunications Engineering, Zhoukou Normal University, Zhoukou 466001, *China*

(Received 24 February 2026; revised manuscript received 11 March 2026; accepted manuscript online 16 March 2026)

This research systematically investigates a three-dimensional nonlinear Schrödinger model with three components featuring partially directionally nonlocal nonlinearities in the presence of harmonic and linear potentials, with applications to nonlinear optics and Bose–Einstein condensates (BECs). To construct optical soliton solutions, we introduce a mapping procedure that establishes a correspondence between the nonautonomous and autonomous models. By rigorously applying the bilinearization technique, we derive analytical solutions for three-component solitons, including one-bright-two-dark ring-shaped single solitons and bi-solitons. We comprehensively analyze their spatiotemporal evolution and partially nonlocal characteristics, with particular emphasis on the formation mechanisms of multilayer and multihump structures governed by the Hermite-polynomial parameter.

Keywords: nonlinear Schrödinger model, one-bright-two-dark ring solitons, partially directional nonlocality

PACS: 05.45.Yv, 42.65.Tg, 42.81.Dp

DOI: 10.1088/1674-1056/ae521b **CSTR:** 32038.14.CPB.ae521b

1. Introduction

Solitons represent a cornerstone of contemporary photonics research, providing profound insights into wave-propagation phenomena in optical fibers,[1,2] laser systems,[3–6] and Bose–Einstein condensates.[7] These shape-preserving wave packets arise from a delicate balance between nonlinearity and dispersion, making them important for both fundamental studies and technological applications. Soliton-like bubbles have also been employed to propel microrobots through cavitation.[8]

The nonlinear Schrödinger (NLS) model[9–12] remains a fundamental model for describing nonlinear optical effects, femtosecond pulse-dispersion management, and information-carrier dynamics in optical communications.[13–16] Recent extensions of the NLS model have incorporated various physical contexts, including synthetic photonic structures,[17] photorefractive crystals,[12] and nonlocal media.[18]

Emerging nonlocal NLS variants have demonstrated remarkable capabilities in modeling soliton dynamics in BECs[19] and nonlinear optical systems.[20] Partially directionally nonlocal (PDN) NLS models introduce partially directionally nonlocal nonlinearities,[21–23] giving rise to higher-dimensional soliton structures, such as Peregrine triple configurations,[21,22] scalar and vector rogue waves,[23] and controllable ring rogue waves.[24,25]

Coupled NLS models enable the description of binary BECs in external potentials[26] and solitons in birefringent fibers.[27] Recent developments include nondegenerate solitons,[27] as well as vector multipole and vortex solitons in cubic[11] and quintic–septimal[9,10] media. Three-component NLS models have also been successfully employed to describe vector solitons,[28] Peregrine solitons,[29] and breathers.[30] However, three-component PDN-NLS models remain largely unexplored despite extensive studies of their two-component counterparts.[21,23,31] This gap motivates the investigation of three-component PDN solitons and may provide further insights into multimode coupling in nonlocal media.

In this work, employing Hirota's bilinear method, we establish a framework for generating diverse ring-soliton structures in individual components of the time-dependent PDL-NLS model

$$\begin{aligned} &\mathrm{i}\frac{\mathrm{d}q_j}{\mathrm{d}t}+a(t)\left(\frac{\mathrm{d}^2q_j}{\mathrm{d}x^2}+\frac{\mathrm{d}^2q_j}{\mathrm{d}y^2}\right)\\ &+b(t)q_j\int_{-\infty}^{+\infty}(|q_1|^2-|q_2|^2-|q_3|^2)\,\mathrm{d}z\\ &+[g(t)(x^2+y^2)+h(t)(x+y)]q_j=\mathrm{i}m(t)q_j, \end{aligned} \tag{1}$$

where $q_j(x,y,t)$, $j=1\sim3$, are complex-valued functions representing either three-component order parameters in ultracold atomic systems or optical field envelopes. Here, x, y, and z denote the spatial coordinates, while t represents the temporal variable. The model features directionally dependent nonlocal nonlinearities modulated by the time-dependent function $b(t)$, exhibiting a local nonlinear response along the x direc-

[†]Corresponding author. E-mail: yangjing0410@126.com

[‡]Corresponding author. E-mail: lijitao@zknu.edu.cn

© 2026 Chinese Physical Society and IOP Publishing Ltd. All rights, including for text and data mining, AI training, and similar technologies, are reserved.

tion and a nonlocal response along the y direction.[22,23] Physically, such nonlocality can arise from distinct mechanisms depending on the system under consideration, including long-range atomic interactions in BECs[19] and nonlocal nonlinear responses in optical media.[20] Other time-dependent parameters include the diffraction-management coefficient $a(t)$, harmonic-potential strength $g(t)$, linear-potential magnitude $h(t)$, and gain/loss modulation $m(t)$. Notably, the two-component special case of Eq. (1) with vanishing external potentials ($g(t)=h(t)=m(t)=0$),[32] as well as the case with vanishing harmonic potential and gain/loss modulation ($g(t)=m(t)=0$),[33] has been investigated previously.

2. Mapping procedure

We introduce the following injective mapping from q_j to Q_j:

$$q_j(x,y,z,t)=\Gamma(z,t)Q_j[\lambda(x,t),\gamma(y,t),\tau(t)]\,\mathrm{e}^{\mathrm{i}\psi(x,y,t)}, \quad (2)$$

under which the time-dependent $(3+1)$-dimensional three-component PDN-NLS system (1) can be transformed into the following autonomous system:

$$\mathrm{i}\frac{\mathrm{d}Q_j}{\mathrm{d}\tau}+\frac{\mathrm{d}^2Q_j}{\mathrm{d}\lambda^2}+\frac{\mathrm{d}^2Q_j}{\mathrm{d}\gamma^2} +2Q_j(|Q_1|^2-|Q_2|^2-|Q_3|^2)=0. \quad (3)$$

Under the specific condition

$$b(t)=2a(t)\,\mathrm{e}^{-2\int_0^t m(t)\,\mathrm{d}t}. \quad (4)$$

The functions in Eq. (2) are given by

(A) Amplitude

$$\Gamma(z,t)=\frac{W_0}{\sqrt{w!2^w\sqrt{\pi}}}H_w(\eta z) \times\exp\left[\int_0^t m(t)\,\mathrm{d}t+4\int_0^t a(t)p(t)\,\mathrm{d}t-\frac{\eta^2}{2}z^2\right], \quad (5)$$

where $H_w(\cdot)$ denotes the Hermite polynomial of order $w(\geq 0)$,[12] with η being a real constant;

(B) Phase

$$\psi(x,y,t)=-p(t)(x^2+y^2)-l(t)(x+y) -2\int_0^t a(t)l(t)^2\,\mathrm{d}t, \quad (6)$$

where the temporal chirp $p(t)$ satisfies $p_t=-g(t)+4a(t)p^2(t)$ and the linear function $l(t)$ satisfies $l_t=-h(t)+4a(t)l(t)p(t)$;

(C) Accumulated time

$$\tau(t)=2W_0^2\int_0^t a(t)\exp\left[8\int_0^t a(t)p(t)\,\mathrm{d}t\right]\mathrm{d}t, \quad (7)$$

(D) Mapping functions

$$\begin{pmatrix}\lambda(x,t)\\ \gamma(y,t)\end{pmatrix}=W_0\left\{\exp\left[4\int_0^t a(t)p(t)\,\mathrm{d}t\right]\begin{pmatrix}x\\ y\end{pmatrix} +2\int_0^t a(t)l(t)\exp\left[4\int_0^t a(t)p(t)\,\mathrm{d}t\right]\mathrm{d}t\right\}, \quad (8)$$

where W_0 denotes the initial width.

3. One-bright-two-dark ring soliton solutions

Rewriting Eq. (2) in polar coordinates, we obtain

$$\mathrm{i}\frac{\mathrm{d}Q_j}{\mathrm{d}\tau}+\frac{\mathrm{d}^2Q_j}{\mathrm{d}r^2}+\frac{1}{r}\frac{\mathrm{d}Q_j}{\mathrm{d}r}+\frac{1}{r^2}\frac{\mathrm{d}^2Q_j}{\mathrm{d}\varphi^2} +2Q_j(|Q_1|^2-|Q_2|^2-|Q_3|^2)=0,\quad j=1\sim 3, \quad (9)$$

where the radius is $r=\sqrt{\lambda^2+\gamma^2}$ and the azimuthal angle is $\varphi=\arctan(\gamma/\lambda)$.

We focus on ring solutions of Eq. (1). For a thin ring with thickness $L\ll R$,[34] two key approximations can be made: (i) the third term in Eq. (9) is negligible, and (ii) the radial dependence $1/r^2$ in the fourth term can be approximated by $1/R^2$.[34] By adopting the ansatz $Q_j=V_j(r,\tau)\,\mathrm{e}^{\mathrm{i}k\varphi}$ with integer $k(>0)$,[34] Eq. (9) can then be approximately reduced to

$$\mathrm{i}\frac{\mathrm{d}V_j}{\mathrm{d}\tau}+\frac{\mathrm{d}^2V_j}{\mathrm{d}r^2}-\frac{k^2}{R^2}V_j+2(|V_1|^2-|V_2|^2-|V_3|^2)V_j=0. \quad (10)$$

For $k\ll R$, Eq. (10) further reduces to

$$\mathrm{i}\frac{\mathrm{d}V_j}{\mathrm{d}\tau}+\frac{\mathrm{d}^2V_j}{\mathrm{d}r^2}+2(|V_1|^2-|V_2|^2-|V_3|^2)V_j=0. \quad (11)$$

Using the bilinearization method for Eq. (11),[29] and in conjunction with the mapping transformation Eq. (2), a family of solutions to Eq. (1) can be obtained.

The approximate one-bright-two-dark soliton solution reads

$$q_j(x,y,z,t)=\frac{W_0}{\sqrt{w!2^w\sqrt{\pi}}}H_w(\eta z)Q_j^{(1,2)}[r,\tau(t)] \times\mathrm{e}^{\int_0^t m(t)\,\mathrm{d}t+4\int_0^t a(t)p(t)\,\mathrm{d}t-\frac{\eta^2}{2}z^2+\mathrm{i}[\psi(x,y,t)+k\varphi]}, \quad (12)$$

where the single-soliton solution is given by $Q_1^{(1)}=\frac{\alpha_1^{(1)}\mathrm{e}^{\varepsilon_1}}{1+\kappa\mathrm{e}^{\varepsilon_1+\varepsilon_1^*}}$, and

$$Q_{s+1}^{(1)}=\frac{\delta_s\mathrm{e}^{\mathrm{i}\xi_s}\left(1-\kappa\frac{u_1-\mathrm{i}v_1}{u_1^*+\mathrm{i}v_1}\mathrm{e}^{\varepsilon_1+\varepsilon_1^*}\right)}{1+\kappa\mathrm{e}^{\varepsilon_1+\varepsilon_1^*}},\quad s=1,2,$$

with

$$\varepsilon_1=u_1r'+\mathrm{i}[u_1^2-2(|\delta_1|^2+|\delta_2|^2)]\tau,$$
$$\xi_s=-[v_s^2+2(|\delta_1|^2+|\delta_2|^2)]\tau+v_sr',$$
$$\kappa=\frac{\sum_{s=1}^2\alpha_1^{(s)}\alpha_1^{(s)*}}{(u_1+u_1^*)^2}\times\left(1-\frac{|\delta_1|^2}{|u_1-\mathrm{i}v_1|^2}-\frac{|\delta_2|^2}{|u_1-\mathrm{i}v_2|^2}\right)^{-1},$$
$$r'=(r-R_0)/L,$$

and the two-soliton solution is given by

$$Q_1^{(2)} = \frac{\alpha_1^{(1)} \mathrm{e}^{\varepsilon_1} + \alpha_2^{(1)} \mathrm{e}^{\varepsilon_2} + \theta_{11} \mathrm{e}^{\varepsilon_1+\varepsilon_1^*+\varepsilon_2} + \theta_{21} \mathrm{e}^{\varepsilon_2+\varepsilon_2^*+\varepsilon_1}}{1 + \nu_{11} \mathrm{e}^{\varepsilon_1+\varepsilon_1^*} + \nu_{12} \mathrm{e}^{\varepsilon_1+\varepsilon_2^*} + \nu_{21} \mathrm{e}^{\varepsilon_2+\varepsilon_1^*} + \nu_{22} \mathrm{e}^{\varepsilon_2+\varepsilon_2^*} + \varpi \mathrm{e}^{\varepsilon_1+\varepsilon_1^*+\varepsilon_2+\varepsilon_2^*}},$$

$$Q_{s+1}^{(2)} = \frac{\delta_s \mathrm{e}^{\mathrm{i}\xi_s}(1 + \omega_{11}^{(s)} \mathrm{e}^{\varepsilon_1+\varepsilon_1^*} + \omega_{12}^{(s)} \mathrm{e}^{\varepsilon_1+\varepsilon_2^*} + \omega_{21}^{(s)} \mathrm{e}^{\varepsilon_2+\varepsilon_1^*} + \omega_{22}^{(s)} \mathrm{e}^{\varepsilon_2+\varepsilon_2^*} + \omega_3^{(s)} \mathrm{e}^{\varepsilon_1+\varepsilon_1^*+\varepsilon_2+\varepsilon_2^*})}{1 + \nu_{11} \mathrm{e}^{\varepsilon_1+\varepsilon_1^*} + \nu_{12} \mathrm{e}^{\varepsilon_1+\varepsilon_2^*} + \nu_{21} \mathrm{e}^{\varepsilon_2+\varepsilon_1^*} + \nu_{22} \mathrm{e}^{\varepsilon_2+\varepsilon_2^*} + \varpi \mathrm{e}^{\varepsilon_1+\varepsilon_1^*+\varepsilon_2+\varepsilon_2^*}}, \quad s = 1,2,$$

with

$$\varepsilon_s = u_s r' + \mathrm{i}[u_s^2 + 2(|\delta_1|^2 + |\delta_2|^2)]\tau,$$

$$\xi_s = -[v_s^2 + 2(|\delta_1|^2 + |\delta_2|^2)]\tau + v_1 r',$$

$$\theta_{11} = (u_2 - u_1)^2 \frac{\nu_{11}\nu_{21}}{\alpha_1^{(1)*}} \upsilon,$$

$$\theta_{21} = (u_2 - u_1)^2 \frac{\nu_{12}\nu_{22}}{\alpha_2^{(1)*}} \upsilon, \quad \omega_{\mathrm{df}}^{(s)} = -\frac{u_d - \mathrm{i}v_s}{u_f^* + \mathrm{i}v_s} \nu_{\mathrm{df}},$$

$$\omega_3^{(s)} = \varpi \frac{(u_1 - \mathrm{i}v_s)(u_2 - \mathrm{i}v_s)}{(u_1^* + \mathrm{i}v_s)(u_2^* + \mathrm{i}v_s)},$$

$$\nu_{\mathrm{df}} = \frac{\alpha_d^{(1)} \alpha_f^{(1)*}}{(u_d + u_f^*)^2} \left[1 - \sum_{c=1}^{2} \frac{|\delta_c|^2}{(u_d - \mathrm{i}v_c)(u_f^* + \mathrm{i}v_c)}\right]^{-1},$$

$$\varpi = |u_2 - u_1|^2 \frac{\nu_{11}\nu_{12}\nu_{21}\nu_{22}}{|\alpha_1^{(1)} \alpha_2^{(1)}|^2} |\upsilon|^2,$$

$$\upsilon = 1 + \sum_{c=1}^{2} \frac{|\delta_c|^2}{(u_1 - \mathrm{i}v_c)(u_2 - \mathrm{i}v_c)},$$

for $d, f = 1, 2$, where $r = \sqrt{\lambda^2 + \gamma^2}$ and $r' = (r - R_0)/L$.

4. PDN property of one-bright-two-dark ring solitons

We analyze the PDN properties of one-bright-two-dark ring solitons under an exponential modulation system[23] described by

$$a(t) = a_0 \exp(-\sigma t), \tag{13}$$

where a_0 and σ denote the initial diffraction coefficient and exponential modulation rate, respectively. Moreover, $p(t) = p_0$ and $l(t) = l_0$ are taken to be constants.

As indicated by the amplitude expression (5), the Hermite polynomial $H_w(\eta z)$ governs the structural variation of the solutions along the z direction. Figure 1(a) shows the amplitude profiles with two ($w = 1$) and three ($w = 2$) characteristic humps corresponding to different polynomial orders. The temporal evolution reveals amplitude enhancement induced by the positive gain coefficient m_0. Meanwhile, Fig. 1(b) shows that the width contracts, while both the effective time and time shift progressively increase with increasing time t. The phase distribution in the xy plane shown in Fig. 1(c) exhibits an inverted parabolic profile, with pronounced phase modulation around the origin ($x = y = 0$), where the phase magnitude varies from its minimum to maximum.

In Fig. 2, we consider one-bright-two-dark ring single solitons with localized properties along the x and y directions. For the bright-ring single soliton of component q_1 shown in Fig. 2(a), a hollow cylindrical shell protrudes from a plane with zero magnitude in the xy plane. For the dark-ring single solitons of components q_2 and q_3 shown in Figs. 2(b) and 2(c), respectively, hollow cylindrical shells are embedded in two planes with relatively large background magnitudes. The magnitude of q_3 is larger than that of q_2 in the xy plane. For the total quantity I shown in Fig. 2(d), the resulting profile resembles that of component q_1 in Fig. 2(a), because the amplitude of q_1 is significantly larger than those of q_2 and q_3. Consequently, the bright component q_1 dominates the contribution of the two dark components q_2 and q_3.

Comparing Fig. 2(a) with Fig. 2(e), we find that, for a fixed thickness L, all one-bright-two-dark ring solitons exhibit increasing radii as R_0 increases. Conversely, for a fixed R_0 (Figs. 2(a) and 2(f)), their thicknesses increase proportionally with the thickness parameter L.

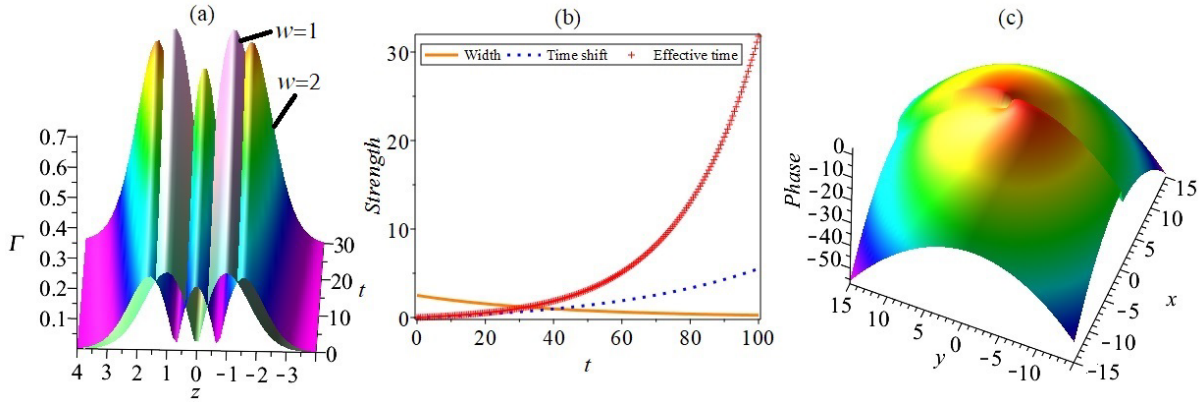


Fig. 1. Characteristics of the solution. (a) Amplitude, (b) variations of the characteristic structural values with time t, and (c) phase at $t = 10$. Parameters: $W_0 = 0.4, \eta = 1, a_0 = 0.05, \sigma = 0.001, m_0 = 0.01, p_0 = 0.12, l_0 = 0.15, w = 0$.

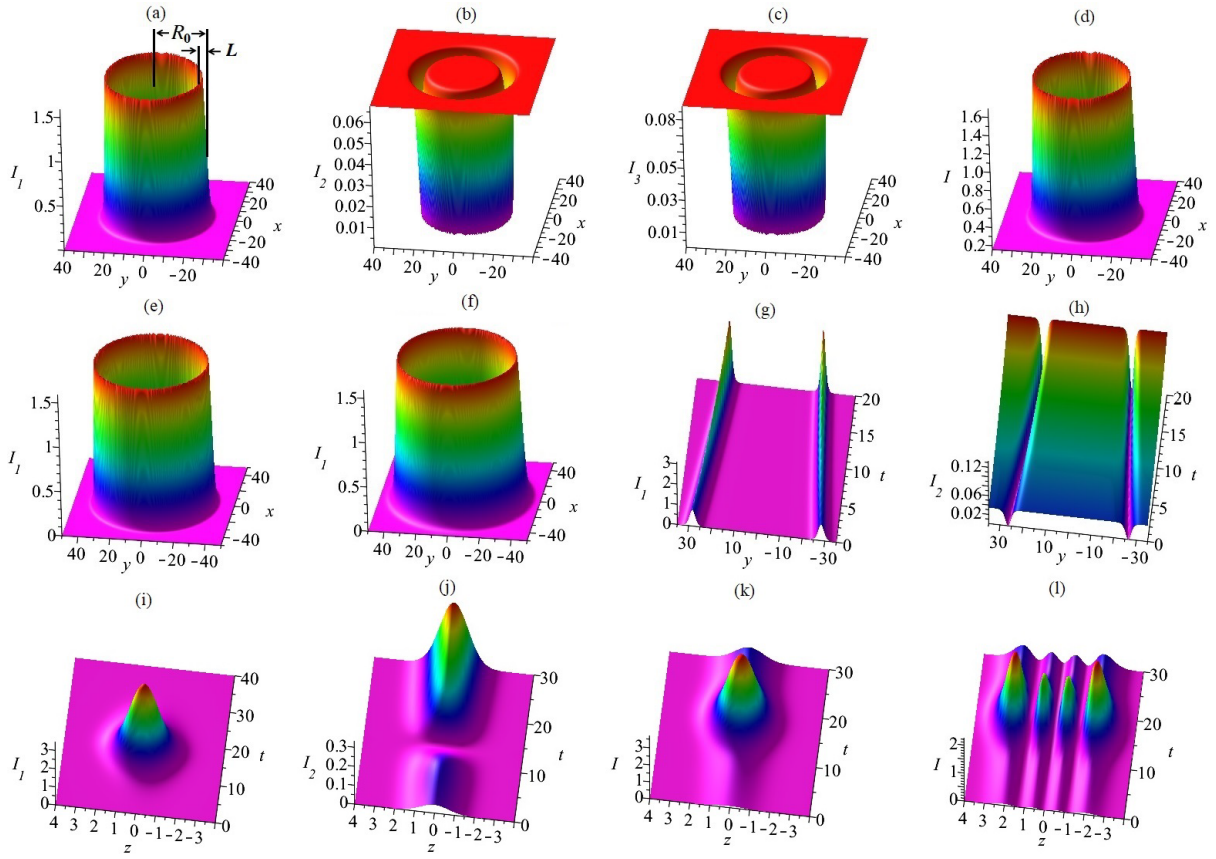


Fig. 2. (a), (e), (f), (g), and (i) Bright, (b), (h), and (j) dark, and (c) dark-ring single-soliton solutions with $I_j = |q_j|^2$, and (d), (k), and (l) total intensity $I = \sum_{j=1}^{3} |q_j|^2$. Panels (a)–(f) show the xy plane at $z = 0.5$ and $t = 10$, panels (g) and (h) show the yt plane at $z = 0.5$ and $x = -0.1$, and panels (i)–(l) show the zt plane at $x = 15$ and $y = 15$. The parameters are the same as those in Fig. 1, with $\alpha_1^{(1)} = 1.25, \delta_1 = 0.7, \delta_2 = 0.8, u_1 = 2, v_1 = 0.2, v_2 = 0.18$, and (a)–(d), (i)–(k) $R_0 = 8, L = 1, w = 0$, (e) $R_0 = 12, L = 1, w = 0$, (f) $R_0 = 12, L = 2, w = 0$, and (l) $R_0 = 8, L = 1, w = 3$.

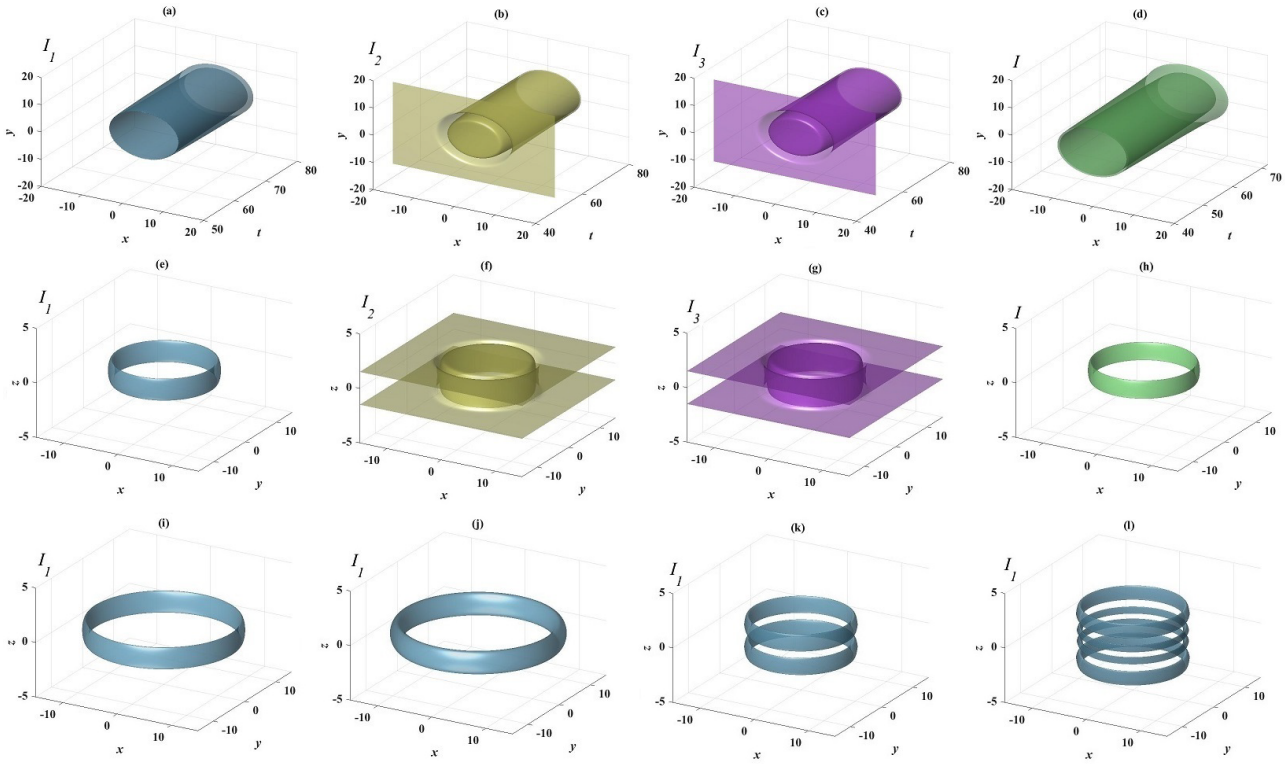


Fig. 3. Isosurface plots for (a), (e), and (i)–(l) bright, (b) and (f) dark, and (c) and (g) dark-ring single-soliton solutions with $I_j = |q_j|^2$, and (d) and (h) total intensity $I = \sum_{j=1}^{3} |q_j|^2$. Panels (a)–(d) show the xyt space at $z = 1$, while panels (e)–(l) show the xyz space at $t = 10$. The parameters are the same as those in Fig. 2, except for (a)–(h) $R_0 = 8, L = 1, w = 0$, (i) $R_0 = 12, L = 1, w = 0$, (j) $R_0 = 12, L = 2, w = 0$, (k) $R_0 = 8, L = 1, w = 1$, and (l) $R_0 = 8, L = 1, w = 3$.

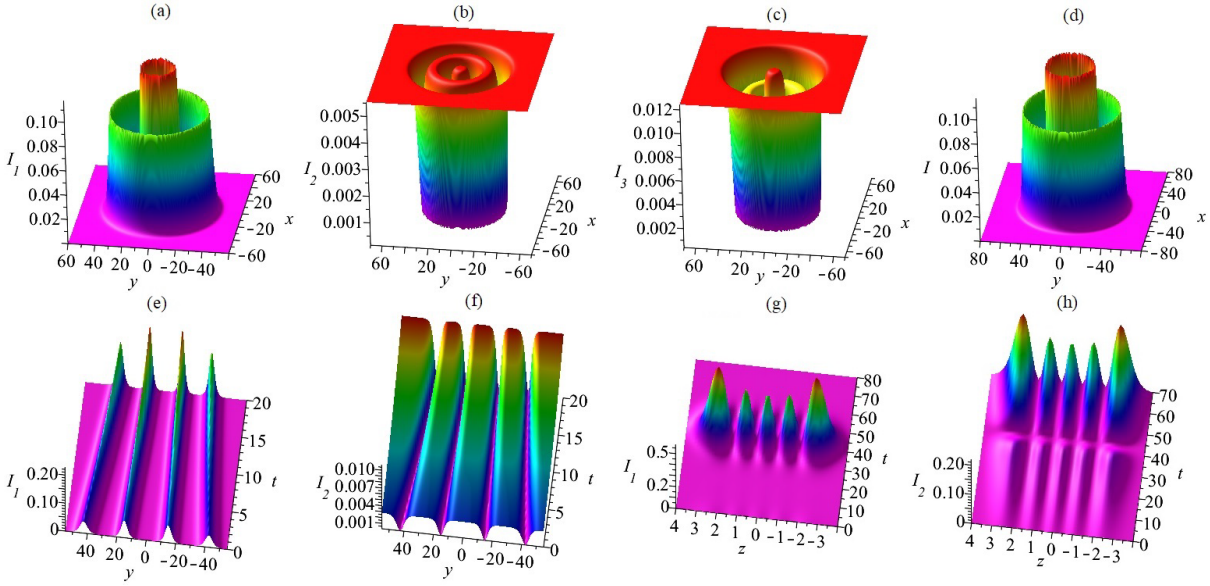


Fig. 4. (a), (e), and (g) Bright, (b), (f), and (h) dark, and (c) dark-ring two-soliton solutions with $I_j = |q_j|^2$, and (d) total intensity $I = \sum_{j=1}^{3} |q_j|^2$. Panels (a)–(d) show the xy plane at $z = 0.5$ and $t = 10$, panels (e) and (f) show the yt plane at $z = 0.5$ and $x = -0.1$, and panels (g) and (h) show the zt plane at $x = 15$ and $y = 15$. The parameters are the same as those in Fig. 1, with $\alpha_1^{(1)} = 1, \alpha_2^{(1)} = 1.5, \delta_1 = 0.2, \delta_2 = 0.3, u_1 = 1.2, u_2 = -1, v_1 = 0.2, v_2 = 0.22, R_0 = 8, L = 1, w = 0$.

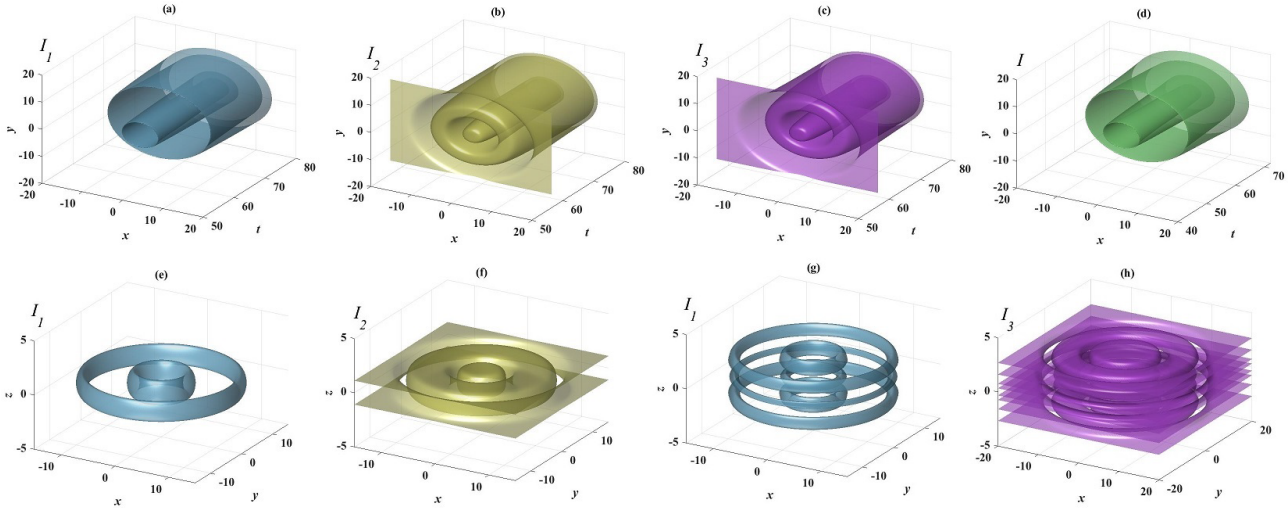


Fig. 5. Isosurface plots for (a), (e), and (g) bright, (b) and (f) dark, and (c) and (h) dark-ring two-soliton solutions with $I_j = |q_j|^2$, and (d) total intensity $I = \sum_{j=1}^{3} |q_j|^2$. Panels (a)–(d) show the xyt space at $z = 1$, while panels (e)–(h) show the xyz space at $t = 10$. The parameters are the same as those in Fig. 4, except for (a)–(f) $w = 0$, (g) $w = 2$, and (h) $w = 3$.

In the yt-plane, the bright ring single-soliton solution q_1 transforms into a dual-peak bright soliton structure (Fig. 2(g)), while the dark ring soliton q_2 evolves into a pair of dark solitons with distinct amplitudes (Fig. 2(h)), and q_3 exhibits a similar structure. In the zt-plane, the bright ring single-soliton solution q_1 exhibits a dromion structure[35] in Fig. 2(i), while the dark ring single-soliton q_2 forms double-depression features on the array-soliton background in Fig. 2(j), and q_3 exhibits a similar structure. The total intensity distribution I in Fig. 2(k) manifests as a composite dromion structure superimposed on the array-soliton background. As the parameter w of the Hermite polynomials increases, the soliton arrays undergo regular proliferation along the z-direction. For $w = 3$, a quadruple-dromion array superimposed on the array-soliton background appears in Fig. 2(l).

Isosurface plots provide a clearer description of the PN properties of the one-bright-two-dark ring solitons. In the xyt space, for the bright component q_1 in Fig. 3(a), a hollow cylindrical shell appears. In contrast, for the dark components q_2 and q_3 in Figs. 3(b) and 3(c), two hollow cylindrical shells are embedded in two distinct planes, respectively. For the total intensity I in Fig. 3(d), the shape is also similar to that of the bright component q_1 in Fig. 3(a).

In the xyz space, a ring appears for the bright component q_1 in Fig. 3(e). In contrast, the dark components q_2 and q_3 in Figs. 3(f) and 3(g) exhibit two dark rings, which separate the space into distinct inner and outer regions. For the total intensity I in Fig. 3(h), the shape is a ring similar to that of

the bright component q_1 in Fig. 3(e). A comprehensive comparison between Figs. 3(e) and 3(i) demonstrates that all one-bright-two-dark ring solitons undergo radial expansion as R_0 increases while maintaining an invariant thickness L. In contrast, when R_0 is held constant, as evidenced by comparing Figs. 3(e) and 3(j), their thicknesses exhibit a linear dependence on the thickness parameter L. As the parameter w of the Hermite polynomials increases, the soliton layers undergo regular proliferation along the z-direction. For $w = 1$ and $w = 3$, two and four layers of rings for the component q_1, respectively, emerge along the z-direction in Figs. 3(k) and 3(l). Along the z-direction, the one-bright-two-dark ring solitons exhibit localization in $(w+1)$ layers of rings for the parameter w.

Finally, Fig. 4 illustrates one-bright-two-dark ring bi-solitons, demonstrating localization in both the x and y directions. Figure 4(a) shows the bright component q_1 forming two nested hollow cylindrical shells protruding from the zero-amplitude xy plane. The dark components q_2 and q_3 in Figs. 4(b) and 4(c) exhibit similar nested shells embedded within distinct finite-amplitude planes, with $q_3 > q_2$ in the xy plane. The total intensity I in Fig. 4(d) resembles that of q_1 because of its dominant amplitude, which offsets the contributions from q_2 and q_3.

In the yt-plane, the bright ring two-soliton solution q_1 evolves into a four-peak structure (Fig. 4(e)), while the dark counterpart q_2 transforms into a dark quad-soliton with distinct amplitudes (Fig. 4(f)), and q_3 exhibits a similar structure. In the zt-plane, when $w = 4$, q_1 forms five dromions (Fig. 4(g)), whereas q_2 generates amplitude depressions on an array-soliton background (Fig. 4(h)), and q_3 exhibits a similar structure. The composite intensity I exhibits five dromions superimposed on this background, similar to the structure shown in Fig. 4(g).

In the xyt-space configuration, distinct features emerge among the soliton components. The bright ring bi-soliton q_1 in Fig. 5(a) manifests as two nested hollow cylindrical shells, while its dark counterpart q_2 in Fig. 5(b) exhibits similar structures embedded within a planar background. Component q_3 displays an analogous dark cylindrical morphology in Fig. 5(c). The total intensity I in Fig. 5(d) replicates the configuration of q_1, with all ring solitons demonstrating radial expansion along the temporal dimension. In the xyz space, q_1 generates nested toroidal rings in Fig. 5(e), whereas q_2 produces dark rings that partition the space into concentric inner, middle, and outer domains in Fig. 5(f), and q_3 exhibits a similar structure. Increasing the Hermite polynomial parameter w induces systematic stratification along the z-direction. For $w = 2$, three-layer nested double rings emerge for q_1 in Fig. 5(g), while for $w = 3$, corresponding four-layer architectures form in Fig. 5(h). This progression confirms the general solution, in which the components localize as $(w+1)$-layer nested double rings along the z-direction.

5. Conclusion

In summary, we have investigated a three-dimensional PDN-NLS model with three components subject to harmonic and linear potentials as well as gain/loss effects. To obtain the soliton solutions, we introduce a mapping procedure that connects the variable-coefficient equations with their constant-coefficient counterparts. By employing the bilinear approach, we derive analytical approximate vector soliton solutions, including one-bright-two-dark ring single-solitons and two-solitons. In the xy-plane, the ring single-solitons form hollow cylindrical shells for the bright component and hollow cylindrical shells embedded asymmetrically in distinct high-amplitude planes for the dark components. The ring two-solitons form two nested hollow cylindrical shells for the bright component and two nested hollow cylindrical shells with distinct planar embeddings for the dark components. In the yt-plane, the ring single-solitons exhibit bright dual-peak and dark bi-soliton structures, while the ring two-solitons evolve into bright and dark quadruple-soliton structures. Along the z-direction, the solutions develop $(w+1)$-dromion structures for the bright component and $(w+1)$-dip structures on array-soliton backgrounds for the dark components, governed by the Hermite parameter w. These findings elucidate the formation mechanisms of multilayer and multi-hump structures and advance the understanding of multicomponent coupled localization in PDN media.

Acknowledgments

This work was supported by the National Natural Science Foundation of China (Grant Nos. 12305006 and 11905308), the Program for Science & Technology Innovation Talents in Universities of Henan Province (Grant No. 25HASTIT025), the Natural Science Foundation of Henan Province (Grant No. 252300420945), and the Research and Practice Project on Higher Education Teaching Reform of Henan Province (Grant No. 2024SJGLX0467).

References

[1] Liu M, Han Y, Liu Q, *et al.* 2025 *Chin. Phys. B* **34** 064202
[2] Cui X N, Zhang Z Y, Liu M W, *et al.* 2025 *Chin. Phys. Lett.* **42** 100402
[3] Si Z Z, Wang D L, Zhu B W, *et al.* 2024 *Laser Photonics Rev.* **18** 2400097
[4] Si Z Z, Ju Z T, Ren L F, *et al.* 2025 *Laser Photonics Rev.* **19** 2401019
[5] Ju Z T, Si Z Z, Yan X, *et al.* 2024 *Chin. Phys. Lett.* **41** 084203
[6] Si Z Z, Ren L F, Wang D L, *et al.* 2025 *Chem. Eng. J.* **505** 159024
[7] Liu J H, Geng K L and Dai C Q 2025 *Chin. Phys. Lett.* **42** 040201
[8] Wang D L, Liu Z X, Zhao H P, *et al.* 2025 *Science* **389** 935
[9] Dai C Q, Wang Y Y, Fan Y, *et al.* 2018 *Nonlinear Dyn.* **92** 1351
[10] Mou D S, Si Z Z, Qiu W X, *et al.* 2025 *Opt. Laser Technol.* **181** 111774
[11] Qiu W X, Geng K L, Zhu B W, *et al.* 2024 *Nonlinear Dyn.* **112** 10215
[12] Dai C Q, Wang Y Y 2020 *Nonlinear Dyn.* **102** 1733

[13] Jia Y H, Si Z Z, Ju Z T, *et al.* 2025 *Sci. China Phys. Mech. Astron.* **68** 284211
[14] Zhang J H, Ju Z T, Wang X P, *et al.* 2025 *Phys. Rev. A* **112** 043518
[15] Si Z Z, Wang Y Y and Dai C Q 2024 *Sci. China Phys. Mech. Astron.* **67** 274211
[16] Ju Z T, Si Z Z, Ren L F, *et al.* 2025 *Opt. Lett.* **50** 1321
[17] Dai C Q, Fan Y and Wang Y Y 2019 *Nonlinear Dyn.* **98** 489
[18] Dai C Q and Zhang J F 2020 *Nonlinear Dyn.* **100** 1621
[19] Sarkar S and Bhattacharyay A 2014 *J. Phys. A: Math. Theor.* **47** 092002
[20] Soljacic M and Segev M 2000 *Phys. Rev. E* **62** 2810
[21] Yang J, Zhu Y, Qin W, *et al.* 2023 *Nonlinear Dyn.* **111** 13287
[22] Yang J, Zhu Y, Qin W, *et al.* 2022 *Nonlinear Dyn.* **108** 2551
[23] Dai C Q, Wang Y Y and Zhang J F 2020 *Nonlinear Dyn.* **102** 379
[24] Zhu Y, Yang J, Chen Z, *et al.* 2024 *Chin. J. Phys.* **91** 784
[25] Chen Y X 2024 *Chaos Solitons Fractals* **180** 114519
[26] Wang L X, Dai C Q, Wen L, *et al.* 2018 *Phys. Rev. A* **97** 063607
[27] Geng K L, Mou D S and Dai C Q 2023 *Nonlinear Dyn.* **111** 603
[28] Vijayajayanthi M, Kanna T and Lakshmanan M 2008 *Phys. Rev. A* **77** 013820
[29] Zhao L C and Liu J 2013 *Phys. Rev. E* **87** 013201
[30] Liu C, Chen S and Akhmediev N 2024 *Phys. Rev. Lett.* **132** 027201
[31] Wu H Y and Jiang L H 2024 *Chaos Solitons Fractals* **182** 114862
[32] Chen L Y and Wu H Y 2025 *Chaos Solitons Fractals* **196** 116384
[33] Chen L and Su S G 2025 *Chaos Solitons Fractals* **199** 116634
[34] Zhong W Y, Qin P, Zhong W P, *et al.* 2022 *Chaos Solitons Fractals* **165** 112824
[35] Zhang B, Zhang X L and Dai C Q 2017 *Nonlinear Dyn.* **87** 2385